Tropical Axisymmetric Mode of Variability in the Atmospheric Circulation: Dynamics as a Neutral Mode

Masahiro Watanabe[1*], Fei–Fei Jin[1], and Masahide Kimoto[2]

1. Department of Meteorology, School of Ocean and Earth Science and Technology
   University of Hawaii at Manoa, Honolulu, HI 96822-2219, USA
2. Center for Climate System Research, University of Tokyo,
   4–6–1 Komaba, Meguro–ku, Tokyo 153–8904, Japan

Corresponding author: Dr. M. Watanabe, E–mail: hiro@soest.hawaii.edu

* On leave from Center for Climate System Research, University of Tokyo.

ABSTRACT

There is an observational evidence that the variability in the global upper tropospheric flow fields on monthly basis is dominated by a zonally uniform pattern symmetric about the equator. This fluctuation is characterized by the zonal–mean zonal wind anomaly having the same sign within the tropics, and thus has been related to changes in the global atmospheric angular momentum. In this paper, mechanism of this variability, referred to as the Tropical Axisymmetric Mode (TAM), was investigated using the NCEP/NCAR reanalysis, an atmospheric general circulation model (AGCM), and a linear baroclinic model.

An index of the TAM, defined by the leading principal component of the observed 300 hPa stream function anomalies, shows quite significant correlation with the Niño 3 SST anomalies, consistent with a well known coherence between the angular momentum and El Niño. While this suggests that the TAM can be forced effectively by El Niño events, data analyses and an AGCM experiment with climatological SSTs show that the TAM appears even in the absence of El Niños, indicating that its origin lies in the atmospheric internal dynamics. A leading singular vector for the zonal mean operator of the linear model, a mode closest to neutrality, indeed resembles well the observed TAM. Furthermore, a considerable part of zonally asymmetric anomalies associated with the TAM can be reproduced as a linear, stationary wave response to the anomalous advection of stationary waves by the zonal–mean flow associated with the near–neutral mode.

Both the neutral mode diagnosis and the TAM of the AGCM reveal that the tropical westerly anomalies are associated with the weakened Hadley cell. The dynamics responsible for persistence of such a mode is mainly the balance between transport of the basic state vorticity and Coriolis force in the zonal momentum budget. Thus, these results indicate that the TAM is essentially identified as a neutral mode of the zonally symmetric atmosphere.

1

1 Introduction

Understanding low–frequency variability in the atmospheric general circulation on time scales longer than that of weather disturbances has so far been one of the major tasks in the climate change studies. For example, it is well known that the so–called teleconnection patterns dominate during the Northern Hemisphere winter season (Wallace and Gutzler 1981; Barnston and Livezey 1987, among others). Tremendous efforts have been made to explain their characteristics in terms of the Rossby wave dispersion (Hoskins and Karoly 1981), effects of zonal asymmetries in the climatological state (Branstator 1990), and interaction between the teleconnection patterns and transient disturbances (Held et al. 1989). On the other hand, the tropical atmosphere reveals anomalies associated with several phenomena: El Niño–Southern Oscillation (ENSO), summer and winter monsoon system, and the Madden–Julian Oscillation (MJO) are especially prevailing over others. A large number of observational and modeling studies have made clear a considerable part of these phenomena (cf. Wallace et al. 1998; Neelin et al. 1998; Webster et al. 1998). Because of higher sea surface temperature (SST) and associated convective activity, the atmospheric fluctuations in the tropics are generally regarded to contain large forced components due to diabatic heating compared to those in the extratropics.

However, there appears to be a dominant pattern of variability in the *global* atmospheric circulation that does not seem to match any of the above phenomena. Lau et al. (1994) and Kang and Lau (1994) applied an empirical orthogonal function (EOF) analysis to the observed, monthly 200 hPa stream function anomalies and showed that the dominant variability is characterized by a near zonally symmetric superrotational flow over the tropics. Zonally symmetric flow patterns similar to the observation are also identified by Branstator (1990) and von Storch (1999) in their atmospheric and coupled general circulation models (AGCM and CGCM), respectively. It is reported that the zonal flow variability is found even in the intraseasonal timescale, associated with the atmospheric angular momentum fluctuations (Anderson and Rosen 1983; Rosen and Salstein 1983; Kang and Lau 1994; Weickmann et al. 1997). This is reasonable because of the two facts that the zonally symmetric variability dominates over the tropics and that the global mean of angular momentum anomalies mostly comes from fluctuations in the tropics (Rosen et al. 1991).

As has been outlined above, various aspects of the principal mode of atmospheric variability which has the zonally symmetric flow pattern have been studied. Nevertheless, the essential dynamics responsible for such a mode is not well explained. Therefore, in this paper we focus on the mechanism of this flow variability in terms of its dynamical origin, using the observational data, an AGCM simulation, and linear model diagnoses. In this study, the zonally symmetric flow variability identified in the previous papers is defined by the leading EOF for the monthly 300 hPa stream function anomalies and referred to as the Tropical Axisymmetric Mode (TAM) throughout the paper. The most important result of this study is that the TAM can be explained by a free mode of the zonally uniform atmosphere, which is the closest to neutrality. The neutral mode, obtained by a modal decomposition of the linear dynamical operator, is considerably reminiscent of the observed TAM in terms of the spatial structure and seasonality.

The TAM, nevertheless, exhibits a significant relationship with El Niños, suggesting that the El Niño excites TAM. The forcing mechanisms of the TAM by El Niño heating will not be detailed in this study, but we have examined the role of zonal flow variability associated with EL Niño in the global teleconnection in a separate study (Watanabe et al. 2001).

This paper is organized as follows. Section 2 introduces the observational data, an AGCM, and a linear model used in this study. The basic features of the observed TAM are presented in section 3, where results of an AGCM simulation with climatological SSTs are also shown in order to verify that the TAM has its origin in the atmosphere's internal dynamics. Section 4 gives the dynamics of the TAM with help of the linear model diagnosis. Discussion and concluding remarks are presented in sections 5 and 6, respectively.

2 Data and Models

a. Observational data

In this study, monthly mean data of various atmospheric fields, derived from the NCEP/NCAR reanalysis (Kalnay et al. 1996), are used. The data are available from January 1949 to December 1999 on a $2.5° \times 2.5°$grid for 17 pressure levels. For the reference variable to identify the TAM, we use the stream function at 300 hPa abbreviated as ψ_{300}. To confirm a good correspondence between TAM and angular momentum as previously reported, the global average of the atmospheric angular momentum over the sphere, denoted as M, is calculated following Rosen et al. (1984),

$$M = \frac{2\pi a^3}{g} \int_p \int_\varphi \overline{u} \cos^2 \varphi d\varphi dp ,$$

where $\overline{u}$ denotes the zonal–mean zonal wind and φ and p are the latitude and pressure, respectively.

We also used SST data, called GISST, provided by the UK Meteorological Office (Parker et al. 1995), in order to define the Niño 3 SST time series as an index for El Niño. While the period of data extends from January 1871 to April 1998, only those after 1949 are used for the analysis.

b. Atmospheric GCM

The AGCM used in this study is a global spectral model cooperatively developed at the Center for Climate System Research (CCSR), University of Tokyo, and the National Institute for Environmental Studies (NIES), referred to as the CCSR/NIES AGCM. The CCSR/NIES AGCM has a standard physics such as the Arakawa–Schubert cumulus parameterization, radiative transfer scheme, a bucket model for land surface processes, the turbulence closure scheme, and the prognostic cloud water scheme (Le Treut and Li 1991). One can find further description of the model in Numaguti et al. (1995) and Shen et al. (1998). In the current version of the CCSR/NIES AGCM, a flux–form semi–Lagrangian scheme (Lin and Rood 1996) has

been applied for the moisture and cloud water transports. The code is parallelized using the standard Message Passing Interface library to save the computational cost.

The model resolution employed here is a triangular truncation with wavenumber 42 (T42) and the vertical 20 levels with σ−coordinate. In order to identify the atmospheric variability dominant in the absence of SST fluctuations, the AGCM has been run for 50 yr with the monthly varying climatological SSTs, and it is referred to as the climatological run hereafter.

c. Linear baroclinic model

We used a linear model, based on the primitive equations identical to those in the CCSR/NIES AGCM, for dynamical analyses. The model has a horizontal resolution of T21 and vertical 20 levels, being expressed by exactly linearized form of equations (see Watanabe and Kimoto 2000, 2001 for detail). Such a linear model can be used in several ways, for example, as a so−called storm track model (Branstator 1995; Watanabe and Kimoto 2000), for time integrations, and for linear budget analyses (Branstator 1992). The budget analysis is also carried out in section 4b. While the linear model does not incorporate physical processes, unlike AGCM, there is another difference of this model from the dynamics of AGCM in dissipation terms that include ∇^4 horizontal diffusion, biharmonic vertical diffusion with the time scale of 1000 day^{-1}. Rayleigh friction and Newtonian damping as represented by a linear drag are also applied to vorticity, divergence, and temperature, with the coefficients fixed at the time scale of 1 day^{-1} for $\sigma \geq 0.9$, 2 day^{-1} for the uppermost two levels, and 20 day^{-1} elsewhere.

With a basic state, denoted as X_c and derived from the NCEP climatology (subscript 'c' stands for climatology), a steady anomalous circulation X_a ('a' denotes anomaly) follows an equation with the matrix form

$$\mathsf{L}(\mathsf{X}_c)\mathsf{X}_a = \mathsf{f} \quad , \tag{1}$$

where f and L indicate a forcing vector and the linear dynamical operator, respectively. Because the rank of L exceeds 30000 in dimensions with this spatial resolution, which is hardly solved by the usual matrix inversion, we replace the basic state X_c by its zonal mean $\overline{\mathsf{X}}_c$ which enables us to decompose Eq.(1) into the zonal mean and stationary wave components as

$$\overline{\mathsf{L}}(\overline{\mathsf{X}}_c)\overline{\mathsf{X}}_a = \overline{\mathsf{f}} + \overline{\mathsf{F}}(\mathsf{X}_a^*, \mathsf{X}_c^*) \quad , \tag{2}$$

$$\mathsf{L}^*(\overline{\mathsf{X}}_c)\mathsf{X}_a^* = \mathsf{F}^*(\overline{\mathsf{X}}_a, \mathsf{X}_c^*) + \mathsf{f}^* \quad , \tag{3}$$

where $\overline{\mathsf{X}}_a, \overline{\mathsf{L}}$, and $\overline{\mathsf{f}}$ are the anomalous zonal mean circulation, its linear operator, and the forcing for anomalous zonal mean equations, while $\mathsf{X}_a^*, \mathsf{L}^*$, and f^* are all for stationary waves. The first term on the right−hand side of Eq.(3) indicates a forcing due to an interaction between the zonal mean anomalies and climatological stationary waves, hereafter referred to as the zonal− wave coupling term. We shall ignore the feedback due to stationary eddy anomalies onto the zonal mean as represented by $\overline{\mathsf{F}}(\mathsf{X}_a^*, \mathsf{X}_c^*)$ in Eq.(2), which is equivalent to the Eliassen−Palm flux divergence, since we found that in the tropics such a feedback is generally not important (see discussion in section 5). Also neglected in Eq.(3) by definition is an interaction between

4

the anomalous and climatological stationary waves $F^*(X_a^*, X_c^*)$, which should be included in Eq.(1). Note that the above two terms are important in forming teleconnection patterns over the northern middle latitudes (Branstator 1992; DeWeaver and Nigam 2000; Kimoto et al. 2001).

Equations (2)–(3) indicate that once the zonal mean anomalies are obtained either as the response to a forcing $\bar{f}$ or by a normal mode analysis of $\overline{L}$, the stationary wave anomalies associated with them can be identified by solving Eq.(3) with relevant forcing due to the zonal–wave coupling. Details for the modal decomposition of $\overline{L}$ will be described in Section 4a. Note that in this study, the stationary wave response X_a^* was truncated with the zonal wavenumber five, since higher wavenumber components were found to less affect the response pattern.

3   Basic features of the zonal flow variability

a. Analyses of observations

As referred to in the introduction, the zonally symmetric flow variability is identified by an EOF analysis for the global, monthly ψ_{300} anomalies[1]. The leading EOF accounts for 23% of the total variance, and shows the zonal structure as found in previous papers (Fig. 1a). The EOF has negligible signals in the extratropics poleward of 40 degrees (not shown), while in the tropics the ψ_{300} anomalies are mostly zonal, corresponding to a superrotational westerly anomaly except for the central Pacific, where a weak twin anticyclone appears. The second and third EOFs (not shown) are also characterized by a zonal flow variability dominant in the extratropics of the Northern and Southern Hemispheres, currently known as the Arctic and Antarctic Oscillations, respectively (e.g. Thompson and Wallace 2000).

Anomalous flow fields associated with this EOF are obtained by regressions upon the principal component of EOF1 (PC1), as displayed in Figs. 1b–1d. The upper level divergence field (Fig. 1b) shows a large–scale feature with the zonal wavenumber one, converging over the maritime continent while diverging over the eastern Pacific–South America. This indicates a displacement of the Walker circulation, which accompanies low–level equatorial westerlies (easterlies) over the Pacific (Indian Ocean) (Figs. 1c and 1d). In addition, the regression map for the surface wind reveals subtropical westerly anomalies especially over the oceans.

As mentioned before, we would like to define the zonally symmetric flow variability, or the TAM, by the EOF1 of ψ_{300} and associated anomaly fields as shown in Fig. 1. Therefore the PC1 used for the regression to obtain the TAM anomalies can be considered as an index of the TAM. Figure 2 presents the TAM index together with the global average of the atmospheric angular momentum, M, and Niño 3 SST anomaly time series. The TAM and M are highly correlated with each other on all timescales, as confirmed by the correlation coefficients higher than 0.8 for both the raw time series and the low–passed time series (Table 1). This implies that the TAM explains a substantial part of the atmospheric angular momentum fluctuations, consistent with Kang and Lau (1994). On the other hand, the correlation between the TAM and Niño 3 SST

---

[1]Because the variability is prevailing in the upper troposphere, results are nearly identical when using a 200 or a 250 hPa stream function field.

anomaly is 0.47, which is relatively low although it is still significant at the 95% level. The lower correlation is probably due to the high–frequency noise in the TAM that is not attributed to the SST fluctuations such as El Niño, since the low–frequency components for both time series show higher correlation of 0.60 (Table 1). Thus it is suggested that the low–frequency behavior of the TAM, and also atmospheric angular momentum, are significantly affected by El Niño events, as has been speculated by Rosen et al. (1984), who found an extremely high value of M during an ENSO warm period in 1983.

Because the TAM is characterized by the zonally symmetric anomalies, its major feature is well captured by the zonal–mean zonal wind anomaly ($\overline{u}_a$) regressed upon the TAM index. Figure 3a shows $\overline{u}_a$ associated with TAM, which represents that the zonal flow anomalies of TAM are relatively barotropic having the same sign throughout the troposphere between 30°S–30°N, and explain nearly half of the local $\overline{u}_a$ variance. The $\overline{u}_a$ associated with El Niño reveals barotropic westerly anomalies as well (Fig. 3b), but they are confined to the subtropics and weak baroclinic anomalies are found on the equator. It should be noted that the fractional variance explained by El Niño–related $\overline{u}_a$ is much smaller than that by $\overline{u}_a$ associated with TAM.

Since the results in Table 1 and Fig. 3 indicate an influence of El Niño on the TAM, we might have to suspect that the TAM is not an independent variability of ENSO, but a part of the ENSO teleconnection pattern. To clarify this question, we replicated the EOF analysis to ψ_{300} anomalies in which El Niño components as defined by the regression anomalies upon the Niño 3 SST anomaly have been subtracted. We confirmed that the EOF1 for such an ENSO–residual fields (denoted as ψ_{300}^R) shows quite similar pattern to Fig. 1a though the fractional variance reduced to 19% (not shown), and that $\overline{u}_a$ regressed upon the PC1 of ψ_{300}^R EOF1 (Fig. 3c) is indeed more similar to $\overline{u}_a$ associated with TAM (Fig. 3a) rather than that associated with ENSO (Fig. 3b). The similarity between Figs. 3a and 3c intimates that the presence of TAM is essentially independent of El Niños, although the temporal behavior appears to be affected by ENSO. Note that the PC1 of the residual field shows a significant correlation with the TAM index and M even though the time series is not correlated with Niño 3 index at all (Table 1). This reinforces the possibility that a considerable part of the TAM and angular momentum variability cannot be explained by El Niños.

To examine the Hadley circulation anomaly associated with $\overline{u}_a$, we showed corresponding zonal–mean meridional wind anomaly, $\overline{v}_a$, in Figs. 3d–3f. The meridional overturning associated with TAM has the maximum on the equator, indicating a single cross–equatorial cell (Fig. 3d), whereas the ENSO–related $\overline{v}_a$ is directed poleward (equatorward) in the upper (lower) troposphere (Fig. 3e). The latter anomaly is consistent with the well–known argument that El Niño accompanies an intensified Hadley cell through the anomalous upward motion on the equator. It should be noted that the meridional flow associated with the ψ_{300}^R EOF1 shows a pattern roughly opposite to the ENSO–related $\overline{v}_a$, i.e., it implies a weakened Hadley circulation (Fig. 3f). It is easily confirmed that the anomalous overturning associated with the TAM index results from the summation of Figs. 3e and 3f, which partially cancel with each other.

The extent to which ENSO contributes to the temporal fluctuation of the TAM may be deduced by comparing the spectral property and persistence between the TAM index and the

6

PC1 of ψ_{300}^R EOF1. The power spectrum of the TAM index shows several peaks (Fig. 4a). While it is not very certain whether the spectral peak at the lowest frequency is reliable because the incorporation of satellite data in the NCEP reanalysis since late 1970s might cause a trend–like bias, the other two are worth noting: one about 4 yr and another about 1 yr periods, respectively. It is interesting to note that the 1 yr peak in the TAM index appears even when the El Niño–related components have been removed (Fig. 4b). The spectral peak of 4 yr arises from an excitation of the TAM due to El Niño, since such a peak disappears in the spectrum for the PC1 of ψ_{300}^R EOF1 (Fig. 4b). The spectral shape in Fig. 4b, which is essentially whiter, further suggests that the SST variability associated with El Niño reddens the spectrum.

Shown in Fig. 5 is the autocorrelation function of the TAM index, a measure of its persistence, which does indicates a quite significant 1 mo lag correlation (above 0.6) and the duration of significance up to the 5 mo lag (solid circles in Fig. 5). The persistence of several months found in the TAM index is clearly much greater than the local persistence of the global ψ_{300} fields which only has one month at most (open circles in Fig. 5). Along with the line of results in previous figures, it is reasonable that the most of this long–lasting feature of the TAM is attributed to the forcing associated with El Niño. Nevertheless, the autocorrelation for the PC1 of ψ_{300}^R (triangles in Fig. 5) still shows greater 1 mo lag correlation than the individual stream function fields, indicating that the TAM may be a persistent mode in the global atmosphere even without the boundary forcing to excite it. Indeed, von Storch (1999) has identified a reddest mode of atmospheric variability in her CGCM similar to the TAM, although it is not very clear the extent to which the SST fluctuations have brought the redness in the model.

b. TAM in an AGCM simulation

Anomalous flow fields associated with the ψ_{300}^R EOF1 showing quite similar structure to the TAM (Fig. 3) suggests that the origin lies in the internal atmospheric dynamics. To verify this, we performed a 50 yr run using the CCSR/NIES AGCM which employed climatological SSTs, as described in section 2b. The EOF1 of the monthly ψ_{300} anomalies derived from the climatological run, and anomaly fields associated with it, are shown in Fig. 6 in a similar manner to Fig. 1. The EOF1 accounts for only 14% of the total variance, which is much smaller than the observational counterpart, but the spatial pattern resembles well the observation (Fig. 6a). The only exception is found over the equatorial Pacific, where the twin anticyclonic anomaly is absent possibly due to no SST variability related to El Niño. While the divergence field has a wavenumber one structure as in the observed TAM, the center is shifted to the west by 60 degrees (Fig. 6b). It is noted that the lower tropospheric flow fields are similar to the observations, exhibiting the divergence over the maritime continent, westerly anomalies over the equatorial Pacific and the subtropical oceans. Strong equatorial westerly anomalies over the central–eastern Pacific found in the observed TAM (Fig. 1d) are not captured by the model. Thus the eastward shift of the Walker circulation associated with the TAM (Figs. 1b and 1d) is not only a consequence of El Niño, although it does look so, but is also a result of the internal mode of the atmosphere.

Further comparison of the AGCM with observation is made after the TAM index of the AGCM was defined by the PC1 of the ψ_{300} EOF as well, referred to as the simulated TAM index. The zonal–mean quantities of $\overline{u}_a$ and $\overline{v}_a$ associated with the sumulated TAM are dis-

7

played in Fig. 7. The simulated TAM accompanies tropical–wide westerly anomalies as in the observation, while the associated meridional flow represents a suppressed Hadley circulation that is reminiscent of the anomalous meridional circulation in the ENSO–residual field (Fig. 3f). Indeed, the power spectrum of the simulated TAM index (not shown) is roughly white in its shape, similar to the spectrum of the observed ψ_{300}^R PC1 (Fig. 4b) but not to that of the TAM index (Fig. 4a).

Although we did not perform another AGCM run with historical SSTs, similarity between Fig. 1 and Fig. 6 lets us expect that the fluctuations in SST do not seriously affect the structure of the TAM. However, the above comparison indicates that the SST variability, especially that related to El Niño, possibly influences the TAM such as to modify the anomalous Hadley circulation and to increase the low–frequency variance. Note that the simulated TAM index also shows a spectral peak near 1 yr period, and an additional peak near 1.5 yr. The spectral peak about 1 yr period found both in the observed and simulated TAMs may imply an active role of the atmospheric annual cycle in generating or modifying the temporal behavior of TAM. Thus the seasonal evolution of the TAM is examined in the next section.

c. Seasonality in the TAM

The atmospheric anomaly fields associated with the TAM such as shown in Figs. 1, 3, and 6 are obtained by the linear regression using all–month data. In this section, the regression is applied for each month to depict the seasonality of the TAM. Since TAM can be represented by $\overline{u}_a$ in the upper troposphere (cf. Fig. 3), the seasonal evolution is first examined with monthly $\overline{u}_a$ at 300 hPa. Shown in Fig. 8a is the time–latitude section of $\overline{u}_a$ associated with the observed TAM. As expected from Fig. 3a, the westerly anomalies cover the tropical band of 30°S–30°N in most months, but there is also an apparent seasonality. Two westerly maxima are found in the figure: one near 20°N in February and another near 15°S in August. The latter maximum anomaly accompanies easterly anomalies to the south. It should be noted that the anomalies almost disappear during November–December. Also an interesting feature in Fig. 8a is that no maximum occurs on the equator, indicating that the tropical $\overline{u}_a$ of the TAM are generated in the off–equatorial latitudes, which was visible in Fig. 3a. A similar cross section is obtained from the simulated TAM, as displayed in Fig. 8b. While the two westerly maxima and a minimum during early winter are reproduced in the AGCM, the maximum in the southern off-equator appears equatorward and in June–July but not in August. This difference may be due to bias in the climatological annual cycle simulated by the AGCM. Causes for the seasonality in the TAM as depicted above will be clarified in section 4b.

While the zonally symmetric components are prevailing in the TAM, it is worth examining the seasonal difference in the zonally asymmetric components associated with TAM, since they may be regarded as a teleconnection pattern related to the TAM. Referring to Fig. 8, we selected two relevant months, i.e. February and August, to show the zonally asymmetric zonal wind anomalies (denoted as u_a^*) at 300 hPa together with $\overline{u}_a$ at the month (Fig. 9). If one focuses on the eastern Pacific, an anticyclonic anomaly dominates over the Northern Hemisphere in February (Fig. 9a) and over the Southern Hemisphere in August (Fig. 9b), consistent with the EOF1 for monthly ψ_{300} (Fig. 1a). Considering the arguments in the previous sections, these anomalies are probably forced by an anomalous heating due to El Niño. When taking a look

at other regions in Fig. 9, several large–scale anomalies are found: a zonally elongated cyclonic anomaly over the North Africa/East Asia and a meridional dipole over the Atlantic, both in February, and subtropical westerly anomalies over southern Africa, Australia, and southern Atlantic, all in August. Interestingly, most of the anomalies are located in latitudes outside the climatological trade winds. The u_a^* associated with TAM generally has larger amplitude in the hemisphere where the $\overline{u}_a$ maximum resides, suggesting that the zonal–wave coupling due to presence of the zonal mean flow anomalies is an important source to excite the stationary eddy anomalies. This possibility can be verified in terms of the dynamics of TAM.

4 Dynamics of the TAM

a. Singular vectors for the zonal mean state

The results shown in the previous section, especially the fact that the AGCM climatological run can simulate a substantial part of the observed TAM, indicate that the variability essentially arises from an internal dynamics of the tropical atmosphere, although it is highly correlated with ENSO. The zonal structure also reminds us that the dynamical origin lies in the zonally uniform states. To test this hypothesis, we calculated singular vectors for the zonal–mean linear operator $\overline{\mathsf{L}}$ in Eq.(2).

Using the Schumit factorization, $\overline{\mathsf{L}}$ can be expressed as

$$\overline{\mathsf{L}} = \mathsf{U}\mathsf{\Sigma}\mathsf{V}^{\mathrm{T}} \quad , \tag{4}$$

where $\mathsf{U} = (\mathsf{u}_1, \mathsf{u}_2, ..., \mathsf{u}_N)$ and $\mathsf{V} = (\mathsf{v}_1, \mathsf{v}_2, ..., \mathsf{v}_N)$ are the orthogonal matrices and called the u–vector and v–vector, respectively. The singular values are contained in a real vector $\mathsf{\Sigma} = (\sigma_1, \sigma_2, ..., \sigma_N)$, corresponding to the absolute value of the complex eigenvalues for $\overline{\mathsf{L}}$. Substituting Eq.(4) into Eq.(2) yields

$$\overline{\mathsf{X}}_a = \sum_i^N \mathsf{v}_i \frac{(\mathsf{u}_i, \overline{\mathsf{f}})}{\sigma_i} \quad . \tag{5}$$

The usefulness of the singular vector analysis for the dynamical operator is summarized in Eq.(5) and has been discussed in earlier works (Navarra 1993; Itoh and Kimoto 1999; Kimoto et al. 2001). Namely, the linear response to *any* forcing is composed by the combination of v–vectors in which the phase and amplitude are determined by the spatial projection of u–vectors onto the forcing divided by the corresponding singular values. In particular, if the forcing is white in space, the response is dominated by the leading mode having the smallest singular value. On this regard, the leading v–vector is referred to as the neutral mode.

Figure 10a shows $\overline{u}_a$ associated with the neutral mode of $\overline{\mathsf{L}}$ when the zonal and annual average of the NCEP climatology was used as the basic state. The singular value of this mode is sufficiently small compared to the other singular modes (not shown), warranting a singularity of the neutral mode. The $\overline{u}_a$ has a broad maximum in the tropics of 30°S–30°N,

with a barotropic structure in the vertical. This pattern remarkably resembles the observed TAM shown in Figs. 3a and/or 3c, and associated $\overline{v}_a$ shown in Fig. 10b reveals an equatorward (poleward) flow in the free troposphere (planetary boundary layer). This weakened Hadley cell again coincides with $\overline{v}_a$ in the observed ENSO–residual field (Fig. 3f) and that in the AGCM (Fig. 7b). One can expect from $\overline{u}_a$ and the associated temperature anomaly showing a warming and cooling over the tropics and subtropics (Fig. 10b) that the mode nearly satisfies the geostrophic balance, although $\overline{v}_a$ indicates the presence of ageostrophic components.

The total structure of the neutral mode presented as a sum of the leading v–vector, v_1, and X_a^* in response to $\mathsf{F}^*(\mathsf{v}_1, \mathsf{X}_c^*)$ (cf. Eq.(3)) reveals some similarity to the observations. Shown in Fig. 11 is the total structure of the neutral mode, which should be compared to the observation (Fig. 1) or the AGCM (Fig. 6). The upper tropospheric flow fields show a strong zonal rotational component and a wavenumber one structure in the divergent component having centers over the Indian Ocean–western Pacific and the eastern Pacific–South America, both of which are in good agreement with the observed and the simulated TAMs. As in TAM of the AGCM, a skew in the ψ_{300} fields does not appear over the central equatorial Pacific, reinforcing that the twin anticyclone in observations (Fig. 1a) indicates a signature associated with ENSO. In the lower troposphere, however, a conspicuous difference is found between the neutral mode and the observed TAM: the positive TAM accompanies strong westerly anomalies over the equatorial Pacific in addition to the subtropics (cf. Figs. 1c and 1d) while they are absent in the neutral mode (Figs. 11c and 11d). Since the simulated TAM also reveals surface wind anomalies along the equator (Fig. 6d), processes which are not included in the linear model may be required for generating the equatorial wind anomalies. The cause of the deficiency of the neutral mode is further discussed in section 5.

Seasonal migration of the observed TAM as shown in Figs. 8 and 9 can be similarly found in the neutral mode structure, repeatedly computed with basic states taken from zonal mean climatology for each month. The maxima in $\overline{u}_a$ at 300 hPa occur in February and August as in the observations, with the centers in the northern and southern off–equators (right panels of Figs. 12a and 12b). Furthermore, it is somewhat surprising that a large part of the zonally asymmetric flow associated with TAM can be reproduced by the stationary wave response to the zonal flow anomaly associated with the neutral mode (Fig. 12). The eddy component as represented by u_a^* agrees with the observed TAM particularly well in February over the subtropics of 0°–180°E and over the tropical Atlantic (Figs. 9a and 12a). Although the stationary eddies in August are less similar to observations, westerly anomalies over the South Atlantic–South Africa are reproduced by the neutral mode as well (Figs. 9b and 12b). The twin anticyclone over the eastern Pacific which exists in the observed TAM (Fig. 9) was not reproduced by the linear model since they are expected to be forced by the diabatic heating associated with El Niños. The result which should be emphasized here is that the zonal asymmetries of the TAM, though in part, are explained by the stationary wave anomalies solely excited by the zonal mean part of the TAM. The cause for the zonal mean part of the TAM is discussed in the next section by examining the dynamics which results in the leading v–vector.

b. Zonal momentum budgets

As shown in Fig. 10, the westerly anomaly of the neutral mode is accompanied by the

equatorial warming and the subtropical cooling. The warming and cooling result adiabatically from the vertical advection, which can be inferred from the meridional wind component showing the descending and ascending motions on the equator and the subtropics, respectively (Fig. 10b). The structure of the neutral mode also suggests that the tropical westerly anomaly coupled with the weakened Hadley cell is of importance for the near–neutral characteristic.

The reason why the coupling of the westerly anomalies with the weaker Hadley circulation is required for the neutrality of the mode becomes apparent when linear budgets are calculated for $\overline{u}_a$ associated with the neutral mode. The curves shown in Fig. 13 are the zonal momentum budgets obtained by substituting $\overline{u}_a$ and $\overline{v}_a$ associated with the neutral mode (Fig. 10) into the linear model. It is shown that the equatorward flow acts to decelerates westerly anomalies through the Coriolis term with the maxima in the subtropics near 30°S and 30°N. At the same time, horizontal advection associated with the meridional flow anomaly works to reinforce $\overline{u}_a$. Mostly due to the cancellation between these two terms, the total tendency (excluding dissipation) is clearly small in the tropics (gray curve in Fig. 13). This is the primary cause for the neutrality of this mode.

The above argument will be clearer when we rewrite a simplified form of the zonal momentum budget as

$$\partial_t \overline{u}_a = f\overline{v}_a - \overline{v}_a \partial_\varphi \overline{u}_c - \overline{\omega}_a \partial_p \overline{u}_c - \alpha \overline{u}_a \ , \tag{6}$$

where f is Coriolis parameter, ∂_φ and ∂_p denote meridional and vertical derivatives, respectively. The damping term is simply represented as $-\alpha\overline{u}_a$. Since the meridional advection apparently depends not only on $\overline{v}_a$ but also on the meridional gradient of the basic state zonal wind (i.e. the basic state vorticity $\overline{\zeta}_c \equiv -\partial_\varphi \overline{u}_c$), it has the maxima around 25°S and 25°N corresponding to the equatorward flank of the subtropical jets (Fig. 13). The vertical advection is relatively small for the neutral mode although it also contributes to enhance $\overline{u}_a$; then the near cancellation of the first two terms leads to the decay rate of $\overline{u}_a$ being solely controlled by the damping term. Indeed, the eigenanalysis of $\overline{\mathsf{L}}$ yields a least damped mode which has the structure quite similar to Fig. 10 and its decay rate is about 17 day^{-1}, which is close to the timescale of the linear damping. We confirmed that the lifetime of the least damped mode is lengthened for weaker damping.

The budget analysis for the zonal momentum of the neutral mode shows that the meridional transport of the basic state vorticity is crucial to the neutral characteristics of the mode. This is reminiscent of the classical theory for the symmetric inertial instability (Emanuel 1979; Dunkerton 1981; Stevens 1983). On the other hand, the condition for symmetric instability, $f(f + \overline{\zeta}_c) < 0$, is not required for the presence of the neutral mode as evident from Fig. 13, showing $f(f + \overline{\zeta}_c)$ positive at any latitude. Since the meridional scale of the mode is determined by the scale of $\overline{\zeta}_c$ which is equivalent to the meridional extent of the subtropical jet, the neutral mode is able to have a large–scale structure of thousand kilometers. The crucial process of the meridional advection of $\overline{\zeta}_c$ also explains the cause of seasonality in the neutral mode hence observed TAM (Fig. 8a). The seasonal cycle of $\overline{\zeta}_c$ coincides well with the seasonal migration of the TAM (Fig. 14) such that $\overline{\zeta}_c$ has a negative minimum near 15°N in February but a positive maximum near 15°S in August, favoring the neutral mode during these months.

11

5 Discussion

As described in the introduction, zonally symmetric mode of variability corresponding to TAM has been found both in observed fields and in GCMs (Branstator 1990; Kang and Lau 1994; von Storch 1999). Thus the results shown in section 3a, in which phenomenological aspects of the TAM were documented, might partially overlap findings in the above articles. What we have focused on is to seek the dynamical origin, and we therefore would like to emphasize that the TAM can be, in essence, explained by the neutral mode of the zonal mean state of the atmosphere.

In the computation of the singular modes, feedbacks due to changes in the stationary eddies and transient disturbances have been ignored (cf. section 2c). Kimoto et al. (2001) have proposed a technique to incorporate the stationary eddy feedback into the zonal mean operator $\overline{\mathsf{L}}$. The leading singular mode of such an operator is a meridional dipole in the northern extratropical westerly, which has been suggested as a prototype of the Arctic Oscillation (Kimoto et al. 2001). In that case, the neutral mode presented here appears as the second mode. Furthermore, we found that the elimination of the stationary eddy feedback is not crucial for the arguments for the neutral mode developed in this study. As for the transient eddy feedback, one may refer to a work by Webster and Holton (1982), who showed that the transient eddies can propagate into the tropics through the so–called westerly duct located in the uppper tropospheric eastern Pacific. While we speculate that the feedback due to such eddies on to the zonal mean flow is not as important as processes examined in this study, it might be worth evaluating the extent to which the anomalous transients affect the tropical zonal–mean flow associated with TAM.

The vertically deep structure of the neutral mode suggests that a similar solution is obtained even with simpler system such as the shallow water equations. In fact, we found a least damped eigenmode of the zonal–mean shallow water equations, which has essentially the same structure (not shown) as the neutral mode shown in Fig. 10. Consistent with results in section 4b, the mode shows larger decay rate when we eliminate the basic state vorticity. It also turned out, however, that the mode itself does not disappear in that case and the overall shape of the eigenspectrum is retained. Thus it seems that the anomalous transport of $\overline{\zeta_c}$ is of importance to cause the neutrality but not crucial for the presence of the mode. We need further investigation to understand the fundamental origin of TAM.

As mentioned in section 4a, low–level flow anomalies associated with the neutral mode much differ from those associated with the observed TAM such that the neutral mode lacks the equatorial westerly (easterly) over the Pacific (Indian Ocean). Since the AGCM can simulate these features relatively well, the surface wind anomaly associated with the TAM might be induced by processes not involved in the linear model. A possible candidate is an interaction between the atmospheric circulation and cumulus convection. To briefly discuss the possibility, we showed a composite difference of the outgoing longwave radiation (OLR) anomalies between positive and negative cases of the observed TAM and the simulated counterpart of the AGCM (Fig. 15). As expected from the significant correlation between the TAM and El Niño, the observed OLR composite shows an enhanced (suppressed) convection over the central Pacific (maritime continent), which is reminiscent of a typical El Niño condition (Fig. 15a). It is

interesting to note that the simulated OLR anomalies also reveal such a pattern although the magnitude is less than half (Fig. 15b). The anomalous convection in the AGCM, which would be induced by the model TAM itself, appears relevant in forcing the surface divergence over the western Pacific (cf. Fig. 6d). It may imply that a two–way feedback has been at work associated with the TAM. The linear model which includes the moisture transport and a cumulus parameterization will enable us to further address this question.

While all the analyses conducted are based on the monthly data, intraseasonal fluctuations associated with the atmospheric angular momentum variability, which share common features with the TAM, have been extensively investigated. As in the neutral mode (Fig. 10), the intraseasonal angular momentum variability reveals tropical westerly anomalies concurrent with a suppressed Hadley circulation (Kang and Lau 1994; Weickmann et al. 1997). Weickmann et al. (1997) have delineated the 30–70 day cycle of the angular momentum variation in terms of the coupling between the tropical zonal wind, Hadley circulation intensity, and convective activity. Because the anomalous convection is moving eastward associated with MJO, the intraseasonal angular momentum anomaly oscillates. On the other hand, the least damped eigenmode of $\overline{L}$ found in this study was stationary. This may not be surprising if the oscillatory nature of the intraseasonal fluctuation comes from an interaction with convection anomalies associated with MJO. Even if so, we believe that the structure in the mature phase of the 30–70 day cycle is derived from the neutral mode dynamics explained in section 4b of this paper because of the similarity to the TAM.

6   Concluding remarks

In the present paper, we have analyzed the TAM, a principal mode of atmospheric variability in the upper tropospheric flow fields, and investigated its dynamical origin. It was shown that the observed TAM reveals the following characteristics, some of which have been noted in earlier papers.

1) The TAM as defined by the leading EOF of the global stream function anomalies has a near zonally symmetric pattern about the equator, except for the central equatorial Pacific where a twin anticyclonic anomaly appears. The essential feature of TAM is well captured by the zonal–mean zonal wind anomalies which have a barotropic structure with the same sign in the tropics (positive TAM corresponds to the tropical westerly anomalies).

2) In association with the TAM, a zonal wavenumber one structure is found in the upper tropospheric divergent field, which accompanies a surface divergence over the maritime continent and westerly anomalies over the equatorial Pacific.

3) The TAM is highly correlated with the atmospheric angular momentum on all the timescales and shows a significant correlation with Niño 3 SST anomalies especially on interannual timescales.

4) The spectral peaks about 1 yr and 4 yr are apparent in the index of TAM, the latter plausibly arising from a forcing associated with El Niño. At the same time, it was suggested that such a SST fluctuation reddens the power spectrum of the TAM.

13

While one might suspect that the TAM is only a response to El Niño because of 3), a 50 yr long AGCM simulation without variability in SSTs does reproduce the spatial structure of the observed TAM not only for 1) but also for 2). Thus the mechanism responsible for the spatial structure of the TAM was suggested to reside in the internal atmospheric dynamics. This was verified by linear model diagnoses, which exhibited that the neutral mode of the zonally uniform atmosphere resembles well the observed TAM in terms of its structure, associated zonal asymmetries, and the seasonality. The neutral character of the mode, hence probably persistence of the observed TAM, was explained by a cancellation between the equatorward transport of the basic state vorticity and Coriolis force, which leads to the minimum zonal–wind tendency in the tropics. The seasonal cycle of the basic state vorticity coincides the seasonal migration of the tropical westerly anomalies associated with the TAM, with the maxima appearing in February and August, reinforcing the above mechanism.

In the present paper, we have not detailed the forcing mechanism of the TAM by El Niño events and the role of TAM in the other phenomena over the tropical–subtropical regions, such as the ENSO teleconnection and monsoons. Some of these issues are examined in a separate study (Watanabe et al. 2001).

14

References

Anderson, J. R., and R. D. Rosen, 1983: The latitude–height structure of 40–50 day variations in atmospheric angular momentum. *J.Atmos.Sci.*, **40**, 1584–1591.

Barnston, A. G., and R. E. Livezey, 1987: Classification, seasonality and persistence of low–frequency atmospheric circulation patterns. *Mon.Wea.Rev.*, **115**, 1083–1126.

Branstator, G., 1990: Low–frequency patterns induced by stationary waves. *J.Atmos.Sci.*, **47**, 629–648.

Branstator, G., 1992: The maintenance of low–frequency atmospheric anomalies. *J.Atmos.Sci.*, **49**, 1924–1945.

Branstator, G., 1995: Organization of storm track anomalies by recurring low–frequency circulation anomalies. *J.Atmos.Sci.*, **52**, 207–226.

DeWeaver, E., and S. Nigam, 2000: Zonal–eddy dynamics of the North Atlantic Oscillation. *J.Climate*, **13**, 3893–3914.

Dunkerton, T. J., 1981: On the inertial stability of the equatorial middle atmosphere. *J.Atmos.Sci.*, **38**, 2354–2364.

Emanuel, K. A., 1979: Inertial instability and mesoscale convective systems. Part I: Linear theory of inertial instability in rotating viscous fluids. *J.Atmos.Sci.*, **36**, 2425–2449.

Held, I. M., S. W. Lyons, and S. Nigam, 1989: Transients and the extratropical response to El Niño. *J.Atmos.Sci.*, **46**, 163–174.

Hoskins, B. J., and D. J. Karoly, 1981: The steady linear response of a spherical atmosphere to thermal and orographical forcing. *J.Atmos.Sci.*, **38**, 1179–1196.

Itoh, H., and M. Kimoto, 1999: Weather regimes, low–frequency oscillations, and principal patterns of variability: A perspective of extratropical low–frequency variability. *J.Atmos.Sci.*, **56**, 2684–2705.

Kalnay, E., M. Kanamitsu, R. Kistler, W. Collins, D. Deaven, L. Gandin, M. Iredell, S. Saha, G. White, J. Woollen, Y. Zhu, M. Chelliah, W. Ebisuzaki, W. Higgins, J. Janowiak, K. C. Mo, C. Ropelewski, J. Wang, A. Leetmaa, R. Reynolds, R. Jenne, and D. Joseph, 1996: The NCEP/NCAR 40–year reanalysis project. *Bull.Amer.Meteor.Soc.*, **77**, 437–471.

Kang, I. S., and K. M. Lau, 1994: Principal modes of atmospheric circulation anomalies associated with global angular momentum fluctuations. *J.Atmos.Sci.*, **51**, 1194–1205.

Kimoto, M., F.-F. Jin, M. Watanabe, and N. Yasutomi, 2001: Zonal–eddy coupling and a neutral mode theory for the Arctic Oscillation. *Geophys.Res.Lett.*, **28**, 737–740.

Lau, K.-M., P.-J. Sheu, and I.-S. Kang, 1994: Multiscale low–frequency circulation modes in the global atmosphere. *J.Atmos.Sci.*, **51**, 1169–1193.

LeTreut, H., and Z.-X. Li, 1991: Sensitivity of an atmospheric general circulation model to prescribed SST changes: feedback effects associated with the simulation of cloud optical properties. *Clim.Dyn.*, **5**, 175–187.

Lin, S.-J., and R. B. Rood, 1996: Multidimensional flux–form semi–Lagrangian transport schems. *Mon.Wea.Rev.*, **124**, 2046–2070.

Navarra, A., 1993: A new set of orthonormal modes for linearized meteorological problems. *J.Atmos.Sci.*, **50**, 2569–2583.

Neelin, J. D., D. S. Battisti, A. C. Hirst, F.-F. Jin, Y. Wakata, T. Yamagata, and S. E. Zebiak, 1998: ENSO theory. *J.Geophys.Res.*, **103**, 14261–14290.

Numaguti, A., M. Takahashi, T. Nakajima, and A. Sumi, 1995: Development of an atmospheric general circulation model. *Climate System Dynamics and Modelling* ed., T. Matsuno, Center for Climate System Research, University of Tokyo, Tokyo, 1–27 [available at CCSR, Univ. Tokyo, 4–6–1 Komaba, Meguro, Tokyo 153–8904].

Parker, D. E., C. K. Folland, A. Bevan, M. N. Ward, M. Jackson, and K. Maskell, 1995: Marine surface data for analysis of climatic fluctuations on interannual to century timescales. *Natural climate variability on decade to century time scales* D.G.Martinson, K.Bryan, M.Ghil, M.M.Hall, T.R.Karl, E.S.Sarachik, S.Soroostian and L.D.Talley, Eds., National Academy Press, 241–250.

Rosen, R. D., and D. A. Salstein, 1983: Variations in atmospheric angular momentum on global and regional scales and the length of day. *J.Geophys.Res.*, **88**, 5451–5470.

Rosen, R. D., D. A. Salstein, T. M. Eubanks, J. O. Dickey, and J. A. Steppe, 1984: An El Niño signal in atmospheric angular momentum and Earth rotation. *Science*, **225**, 411–414.

Rosen, R. D., D. A. Salstein, and T. M. Wood, 1991: Zonal contributions to global momentum variations on intraseasonal through interannual time scales. *J.Geophys.Res.*, **96**, 5145–5151.

Shen, X., M. Kimoto, and A. Sumi, 1998: Role of land surface processes associated with interannual variability of broad–scale Asian summer monsoon as simulated by the CCSR/NIES AGCM. *J.Meteor.Soc.Japan*, **76**, 217–236.

Stevens, D. E., 1983: On the symmetric stability and instability of zonal mean flows near the equator. *J.Atmos.Sci.*, **40**, 882–893.

Thompson, D. W. J., and J. M. Wallace, 2000: Annular modes in the extratropical circulation. Part I: Month–to–month variability. *J.Climate*, **13**, 1000–1016.

vonStorch, J. S., 1999: The reddest atmospheric modes and the forcings of the spectra of these modes. *J.Atmos.Sci.*, **56**, 1614–1626.

Wallace, J. M., and D. S. Gutzler, 1981: Teleconnections in the geopotential height field during the Northern Hemisphere winter. *Mon.Wea.Rev.*, **109**, 784–812.

Wallace, J. M., E. M. Rasmusson, T. P. Mitchell, V. E. Kausky, E. S. Sarachik, and H. von Storch, 1998: On the structure and evolution of ENSO–related climate variability in the tropical Pacific: Lessons from TOGA. *J.Geophys.Res.*, **103**, 14241–14259.

Watanabe, M., and M. Kimoto, 2000: Atmosphere–ocean thermal coupling in the North Atlantic: A positive feedback. *Quart.J.R.Met.Soc.*, **126**, 3343–3369.

Watanabe, M., and M. Kimoto, 2001: Corrigendum. *Quart.J.R.Met.Soc.*, **127**, 733–734.

Watanabe, M., M. Kimoto, and F.-F. Jin, 2001: Role of zonal flow variability in the upstream ENSO teleconnection. *J.Climate*, submitted.

Webster, P. J., and J. R. Holton, 1982: Cross-equatorial response to middle-latitude forcing in a zonally varying basic state. *J.Atmos.Sci.*, **39**, 722–733.

Webster, P. J., V. O. M. na, T. N. Palmer, J. Shukla, R. A. Tomas, M. Yanai, and T. Yasunari, 1998: Monsoons: Processes, predictability, and prospects for prediction. *J.Geophys.Res.*, **103**, 14451–14510.

Weickmann, K. M., G. N. Kiladis, and P. D. Sardeshmukh, 1997: The dynamics of intraseasonal atmospheric angular momentum oscillations. *J.Atmos.Sci.*, **54**, 1445–1461.

Table 1. Correlation coefficients between the time series shown in Fig. 2. Values in brackets denote coefficients between the low–pass filtered time series which retained time scales longer than 24 months. Correlations with the PC1 for the ENSO–residual stream function (ψ_{300}^R) are also indicated.

	ψ_{300} PC1	ψ_{300}^R PC1	M	Niño 3 SST
ψ_{300} PC1	1.0	0.86	0.83	0.47
		(0.74)	(0.80)	(0.60)
ψ_{300}^R PC1		1.0	0.62	0.00
			(0.40)	(0.00)
M			1.0	0.57
				(0.67)
Niño 3 SST anomaly				1.0
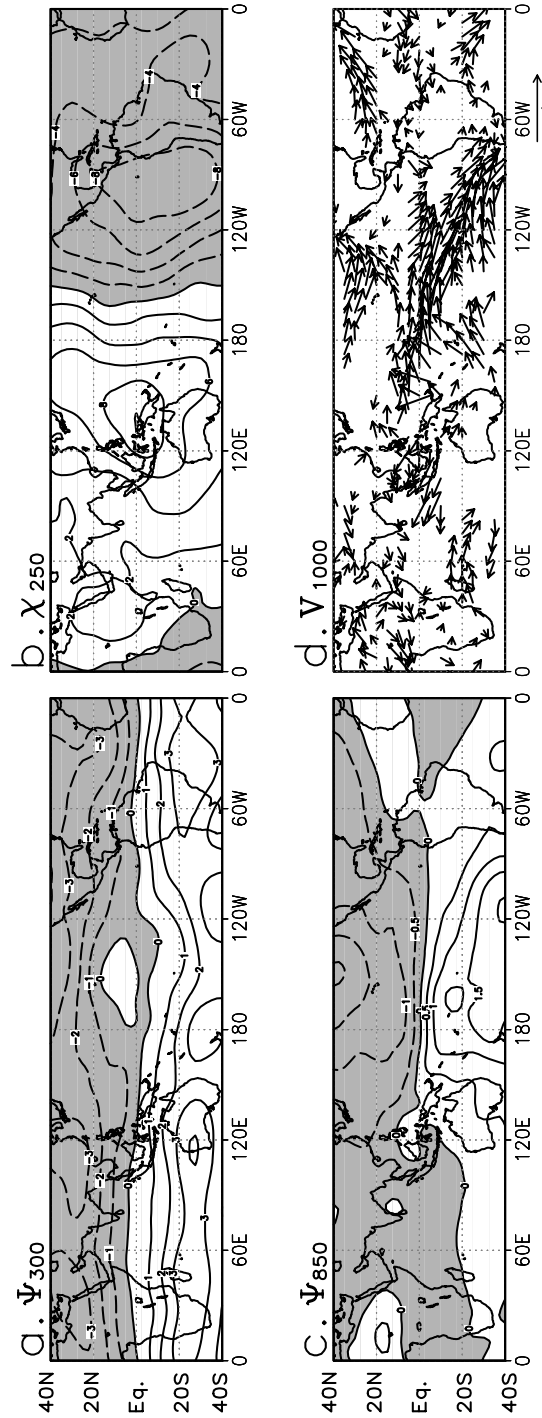
Fig.1 Regression of monthly (a) stream function anomalies at 300 hPa, (b) velocity potential anomalies at 250 hPa, (c) stream function anomalies at 850 hPa, and (d) wind anomalies at 1000 hPa on the leading PC of 300 hPa stream function (23% of the total variance) derived from the NCEP reanalysis fields for 1949–1999. The contour intervals are 1×10^6, 1×10^5, and 0.5×10^6 m^2 s^{-1} for (a)–(c), respectively, and all the panels correspond to one standard deviation of the PC1. The negative values are shaded.

21
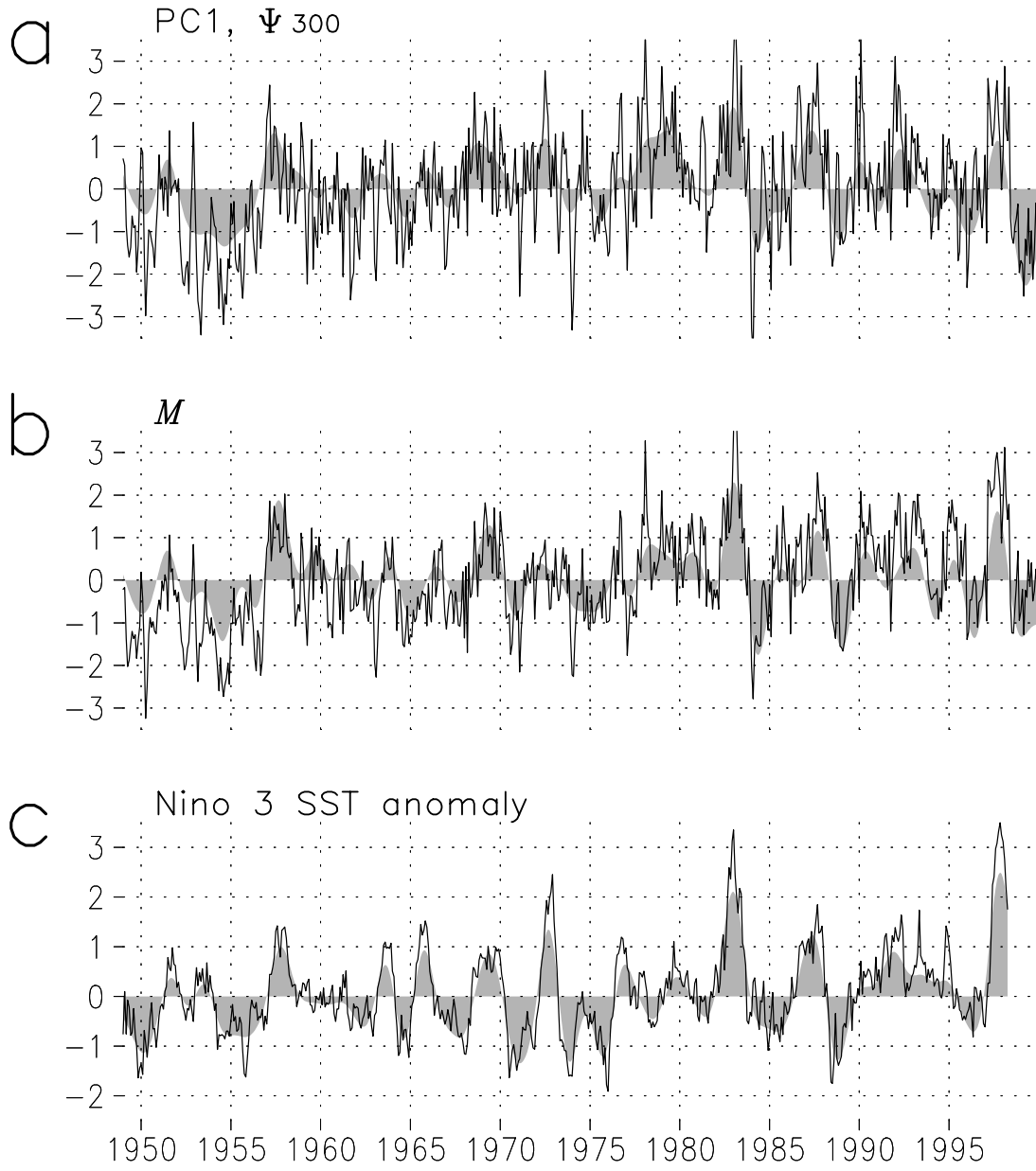
Fig.2 Time series of (a) the TAM index as defined by ψ_{300} PC1, (b) global atmospheric angular momentum, and (c) the Niño 3 SST anomaly. Units for (b) and (c) are respectively 10^{25} kg m^2 s^{-1} and K. The 24 mo low pass filtered components are represented by shading.
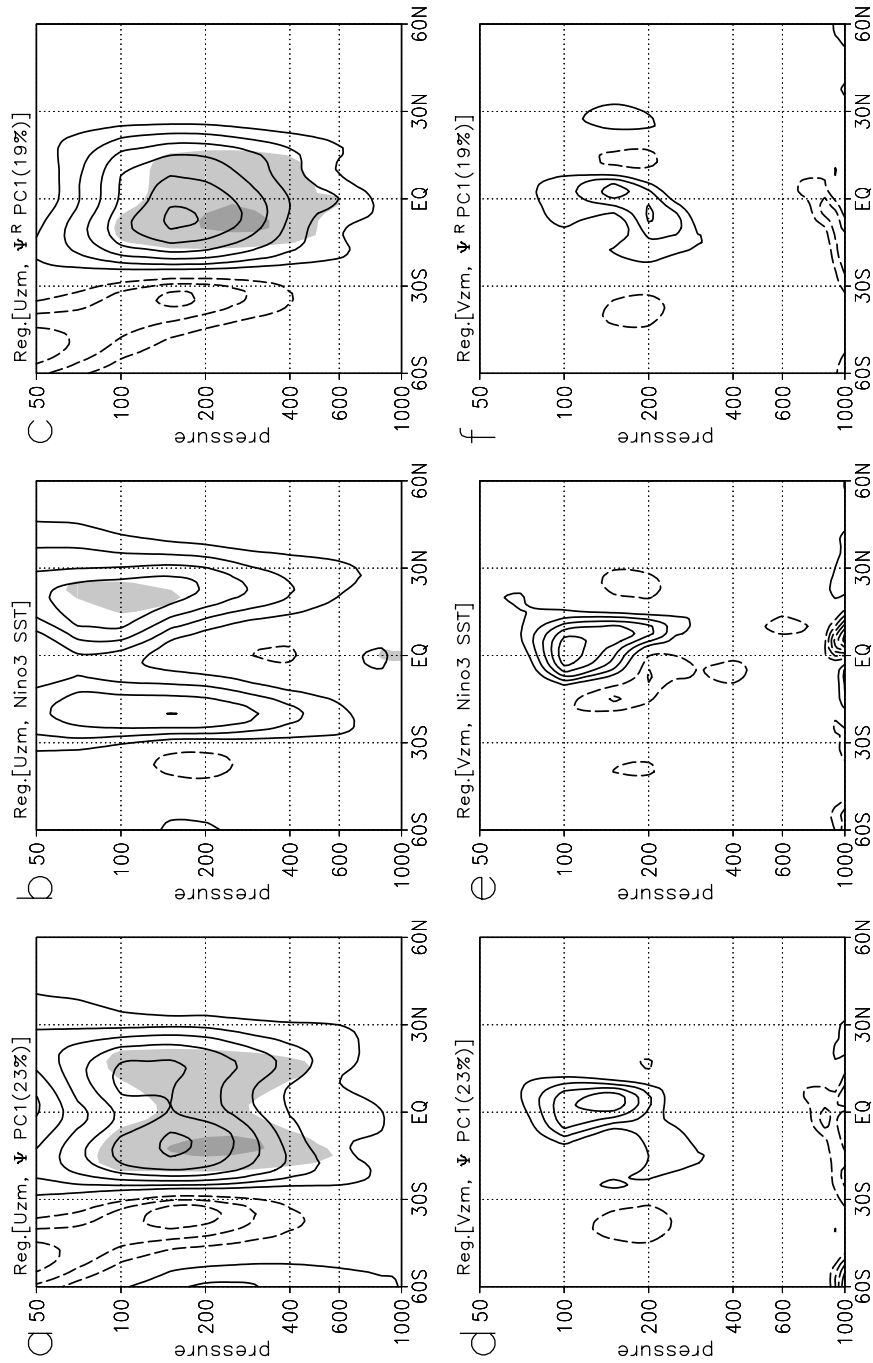
Fig.3 Regression of monthly zonal–mean zonal wind against (a) the TAM index, (b) Niño 3 SST anomaly, and (c) the leading PC of 300 hPa residual stream function (in which El Niño–related anomalies excluded). The contour interval is 0.3 m s^{-1} while negative contours are dashed. The light (dark) shadings indicate regions where local variance fraction exceeds 30% (60%). (d)–(f) As in (a)–(c), except for the zonal–mean meridional wind. The contour interval is 0.02 m s^{-1}.
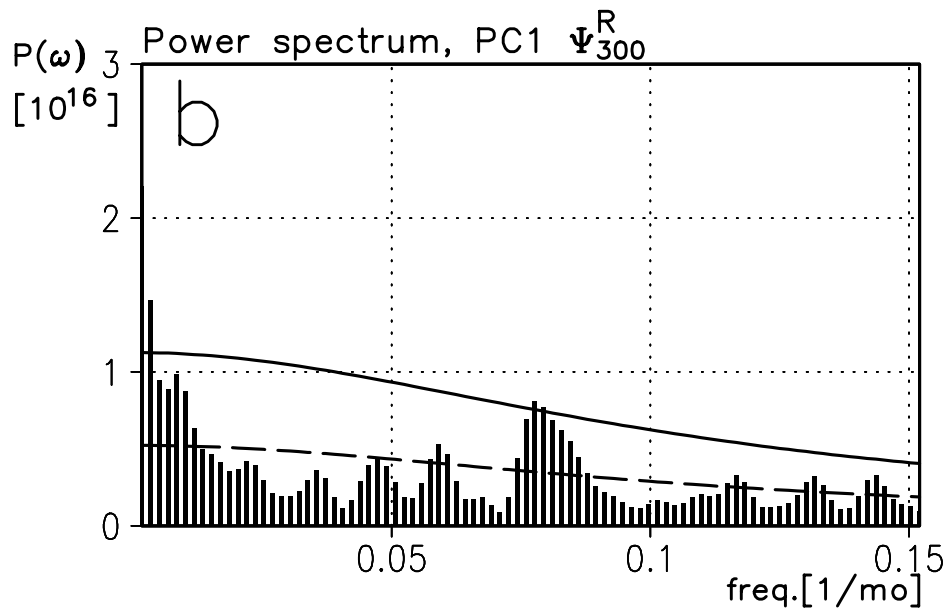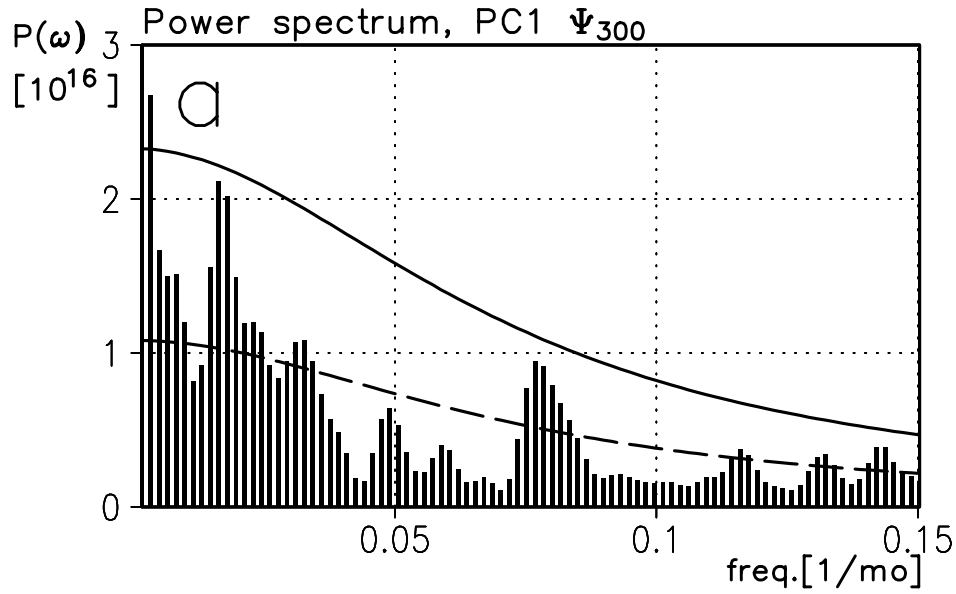
Fig.4 (a) Power spectrum of the TAM index time series shown in Fig. 3a. Corresponding red noise spectrum and the 95% limit are indicated by dashed and solid lines, respectively. (b) As in (a), except for the spectrum of the PC1 for ψ_{300}^R.
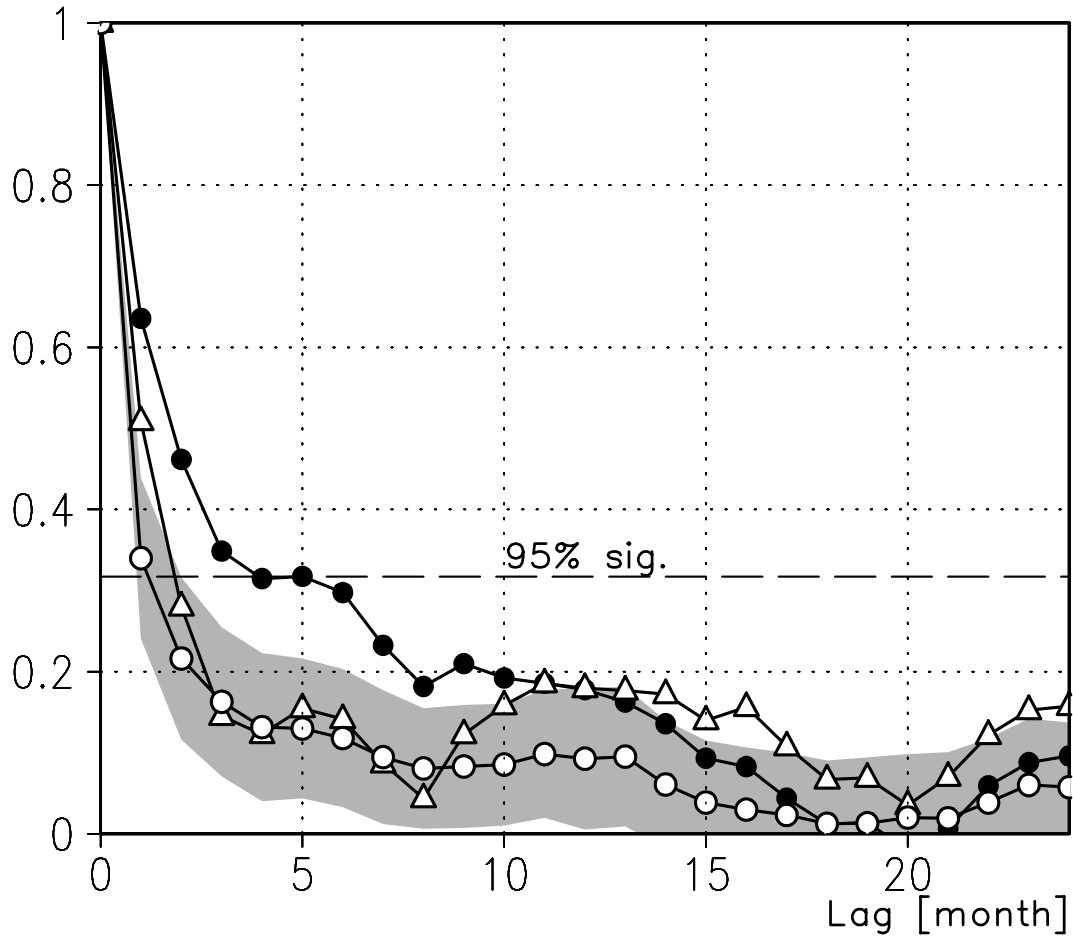
Fig.5 (a) Autocorrelations for the monthly TAM index time series (closed circle), the PC1 for ψ_{300}^{R} (triangle), and a global average of pointwise 300 hPa stream function anomalies (open circle), all with lags in months. Shading denotes one standard deviation of the autocorrelation functions for individual grid. The 95% significance level is shown by the dashed line.
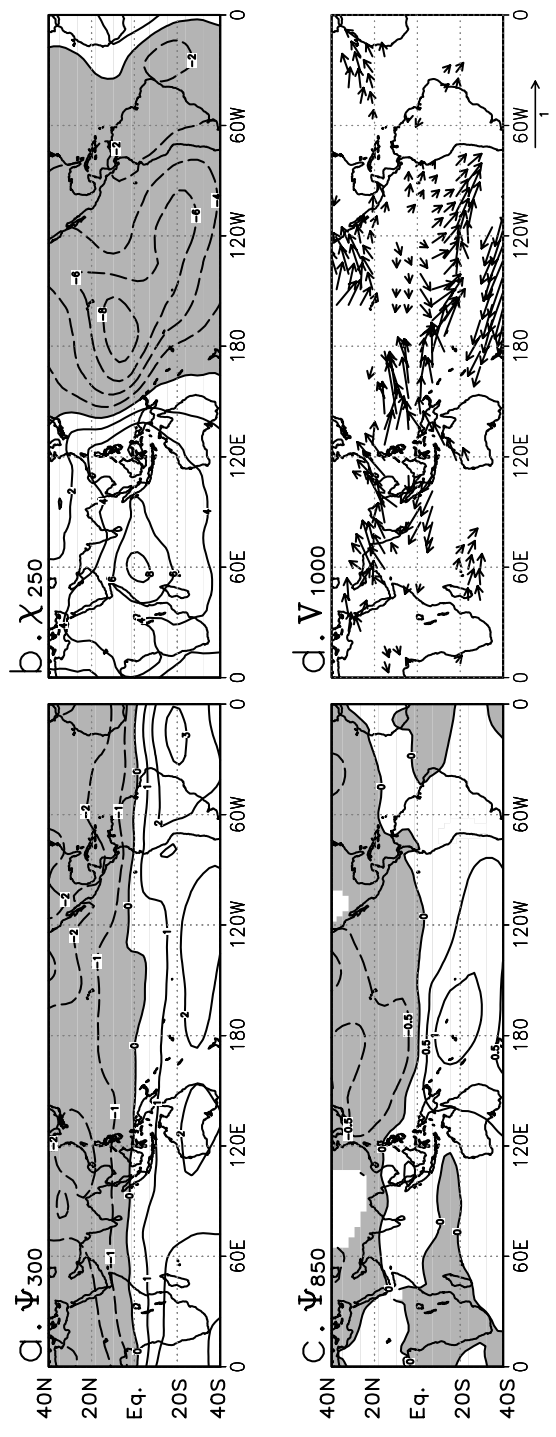
Fig.6 As in Fig. 1, except for a 50 yr AGCM run with climatological SSTs.
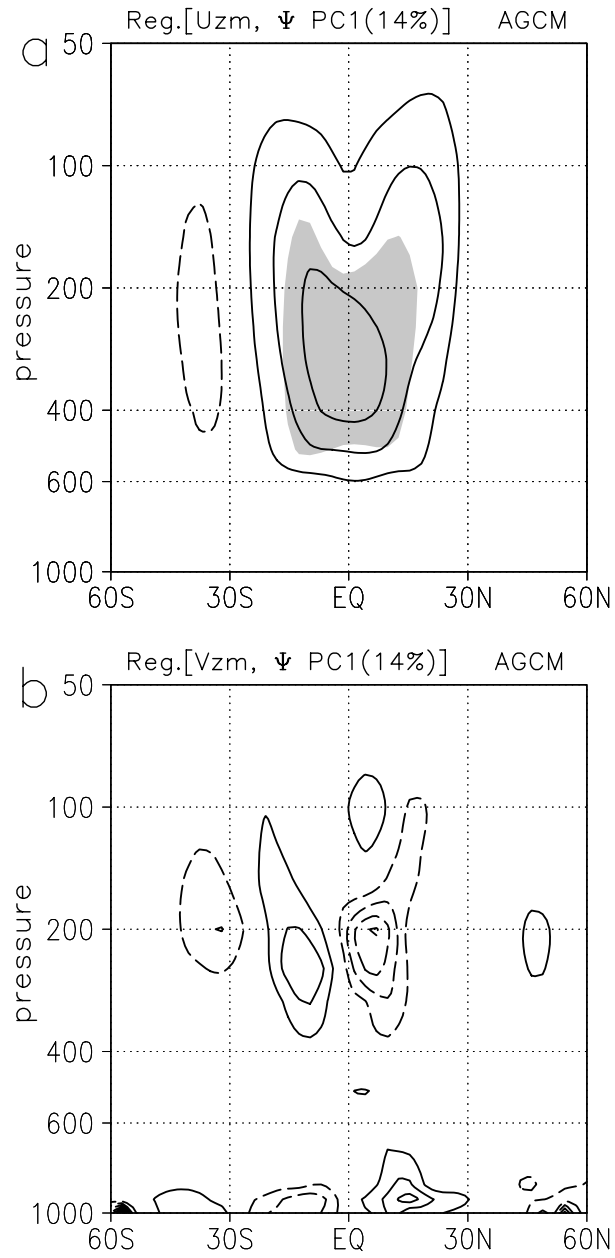
Fig.7 As in Figs. 3a and 3d, except for the 50 yr AGCM run.
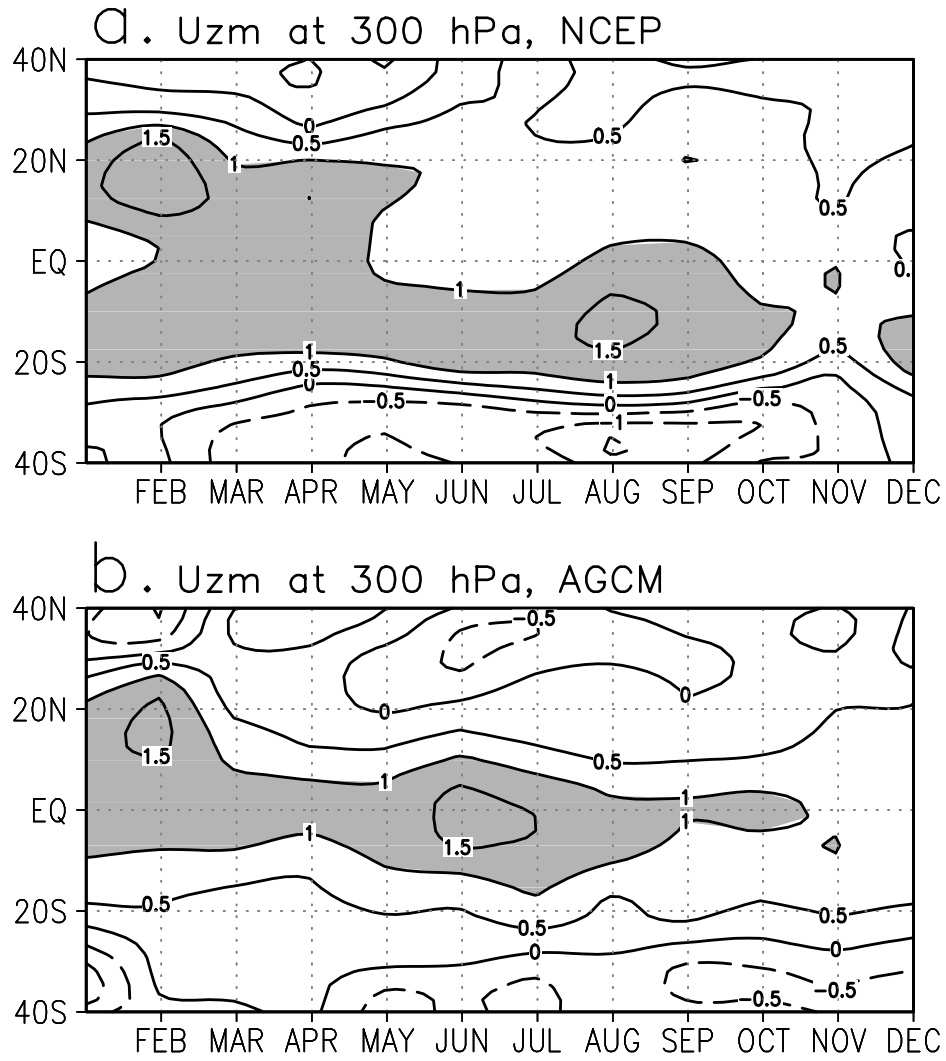
Fig.8 (a) Seasonal evolution of $\overline{u}_a$ at 300 hPa associated with the TAM. The contour interval is 0.5 m s^{-1} and negative contours are dashed. Westerly anomalies greater than 1 m s^{-1} are shaded. (b) As in (a), except for the AGCM run.
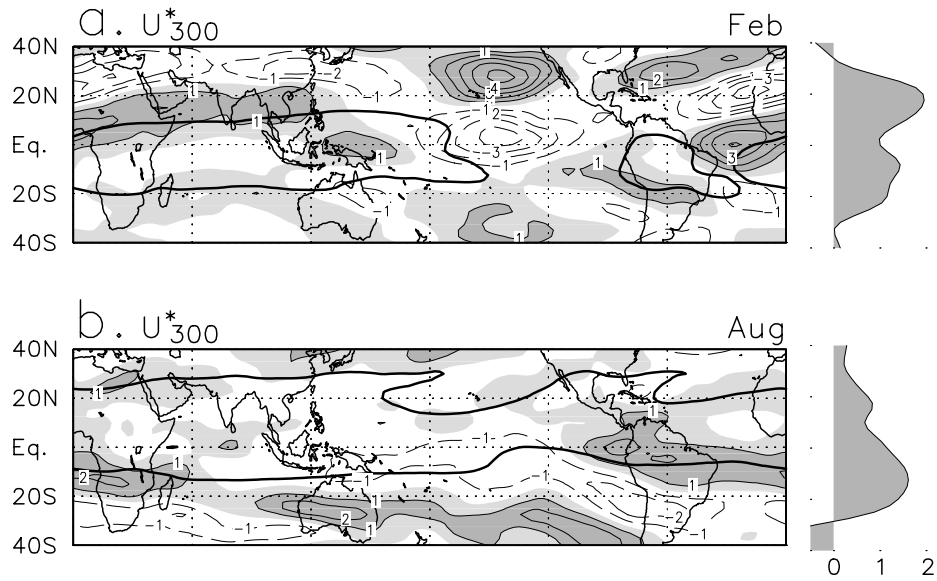
Fig.9 Zonally asymmetric components of the observed 300 hPa zonal wind anomalies (thin contours) associated with the TAM in (a) February, (b) August. The contour interval is 1 m s^{-1}, zero contours omitted. Regions of westerly anomalies (more than 1 m s^{-1}) are shown by the light (dark) shading. The zero contours for the climatological zonal wind are superimposed by thick solid lines. Zonal–mean zonal wind anomalies (m s^{-1}) associated with each map are also shown in the right panels.
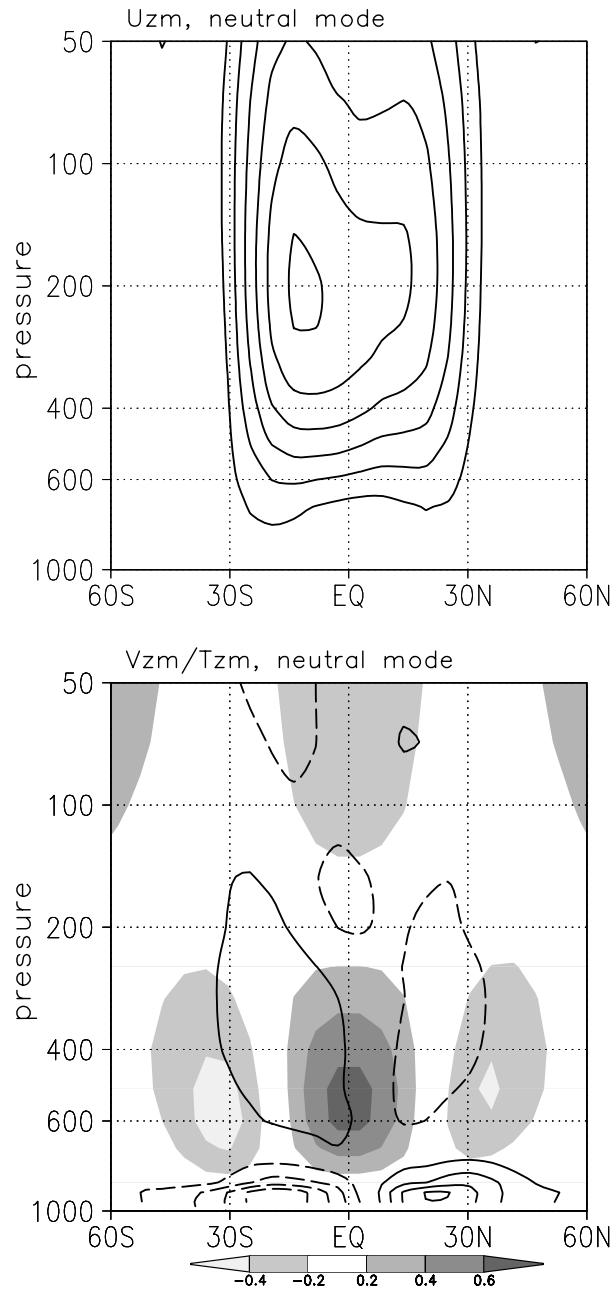
Fig.10 Neutral mode of the zonal–mean operator of the linear model, as represented by (a) zonal wind and (b) meridional wind (contour) and temperature (shading). The contour intervals are 0.6 and 0.02 m s^{-1} for (a) and (b), respectively.
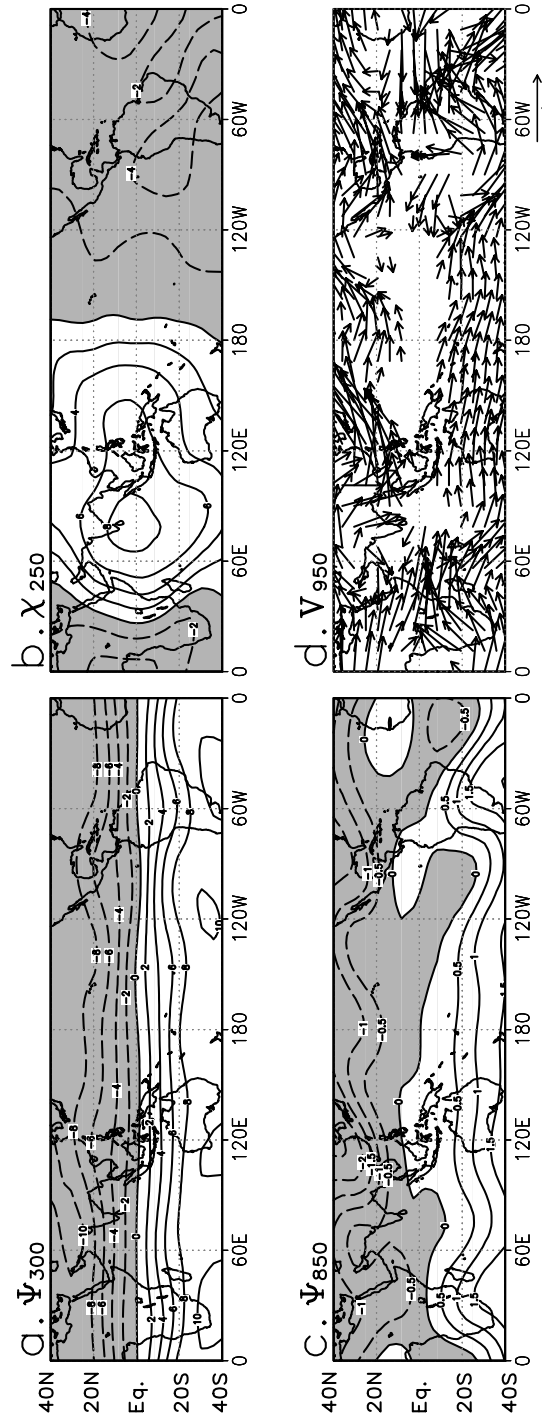
Fig.11 As in Fig. 1, except for the neutral mode and associated zonally asymmetric responses. The contour interval is 2×10^6 m^2 s^{-1} for (a).
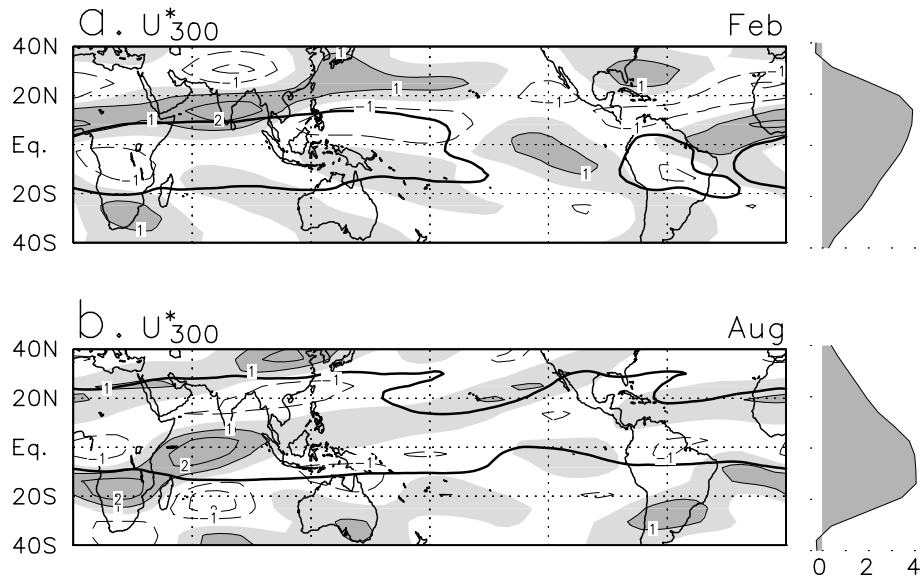
Fig.12 As in Fig. 9, except for stationary wave responses to forcing due to coupling between the neutral mode and climatological stationary waves. Only the basic state and climatological waves are different between (a) and (b). Shown in the right panels are zonal wind associated with the neutral modes for the respective month.
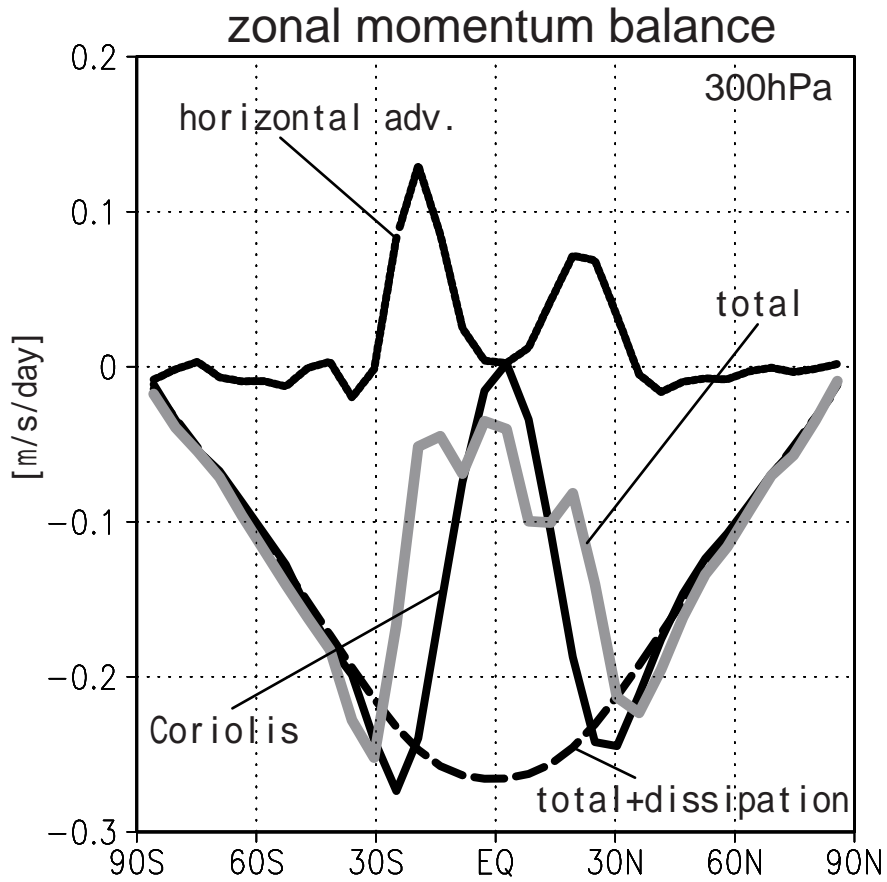
zonal momentum balance

Fig.13 Linear budgets for the 300 hPa zonal momentum associated with the neutral mode shown in Fig. 10. Each curve is represented as the zonal wind acceleration rate of m s^{-1} da $\bar{y}^{-1}$. Note that the 'total' accounts for summation of all the terms except for the dissipation term.
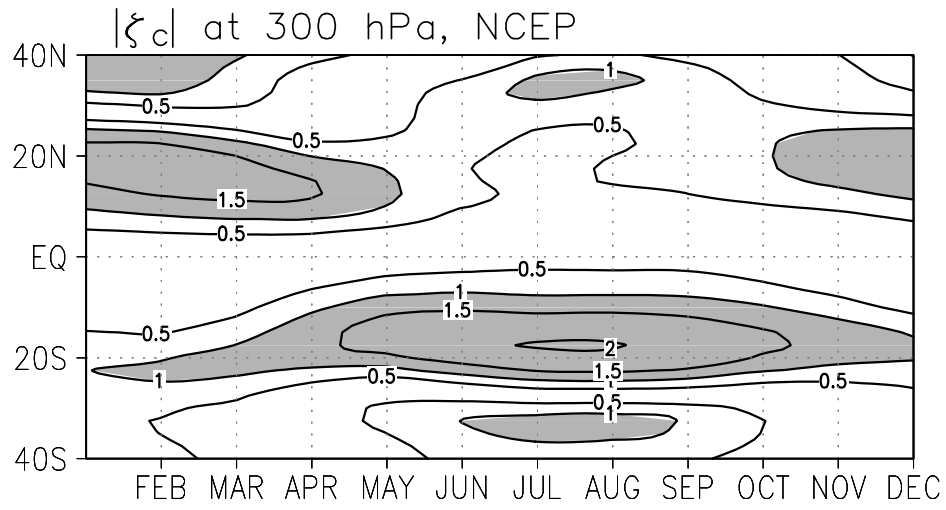
Fig.14 Absolute values of the observed climatological vorticity at 300 hPa. The contour interval is 0.5 $\times 10^{-5}$ s^{-1} and regions greater than 1×10^{-5} s^{-1} are shaded.
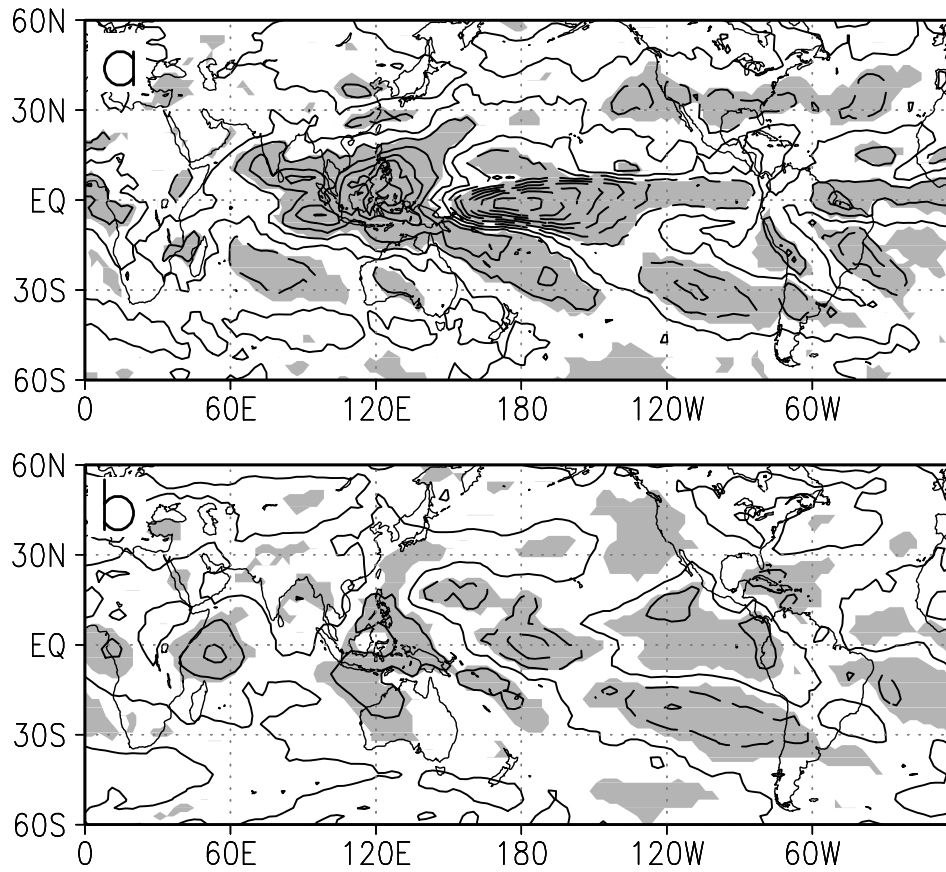
Fig.15 (a) Composite anomalies of observed OLR associated with the TAM index. The OLR data are derived from NOAA satellites and available from June 1974 to November 1998. The contour interval is 5 W m^{-2} and the significant anomaly at the 95% level is denoted by shading. (b) As in (a), except for the composite anomalies in the 50 yr AGCM simulation.